J. Fluid Mech. (2025), *vol.* 1017, A12, doi:10.1017/jfm.2025.10413

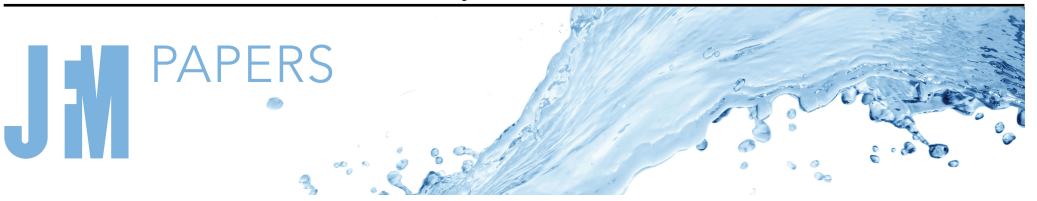

Asymmetric equilibrium states for melting and freezing in thermal convection

Rui Yang[1,2], **Dehao Xu**[2], **Roberto Verzicco**[2,3,4] and **Detlef Lohse**[2,5]

[1]Department of Mechanical and Aerospace Engineering, Princeton University, Princeton, NJ 08544, USA

[2]Physics of Fluids Group and Max Planck Center for Complex Fluid Dynamics, and JM Burgers Centre for Fluid Dynamics, University of Twente, P.O. Box 217, 7500AE, Enschede, The Netherlands

[3]Dipartimento di Ingegneria Industriale, University of Rome Tor Vergata, Roma 00133, Italy

[4]Gran Sasso Science Institute Viale F. Crispi, L'Aquila 7, 67100, Italy

[5]Max Planck Institute for Dynamics and Self-Organization, 37077 Göttingen, Germany

Corresponding authors: Rui Yang, ruiyang@princeton.edu; Detlef Lohse, lohse.jfm.tnw@utwente.nl

(Received 24 December 2024; revised 20 April 2025; accepted 25 June 2025)

A block of ice in a box heated from below and cooled from above can (partially) melt. Vice versa, a box of water with less heating from below or more cooling from above can (partially) re-solidify. This study investigates the asymmetric behaviours between such melting and freezing processes in this Rayleigh–Bénard geometry, focusing on differences in equilibrium flow structures, solid–liquid interface morphology, and equilibrium mean interface height. Our findings reveal a robust asymmetry across a range of Rayleigh numbers and top cooling temperature (i.e. hysteretic behaviour), where the evolution of freezing shows a unique 'splitting event' of convection cells that leads to a non-monotonic height evolution trend. To characterise the differences between melting and freezing, we introduce an effective Rayleigh number and the aspect ratio for the cellular structures, and apply the heat flux balance and the Grossmann–Lohse theory. Based on this, we develop a unifying model for the melting and freezing behaviour across various conditions, accurately predicting equilibrium states for both phase-change processes. This work provides insights into the role of convective dynamics in phase-change symmetry-breaking, offering a framework applicable to diverse systems involving melting and freezing.

Key words: Bénard convection, solidification/melting

1. Introduction

Melting and freezing in the presence of turbulent flows are fundamental processes in both natural and industrial settings, with wide-ranging applications, including the evolution of polar ice (Stanton *et al.* 2013; Dutrieux *et al.* 2014; Cenedese & Straneo 2023), magma oceans (Labrosse, Hernlund & Coltice 2007; Alboussiere, Deguen & Melzani 2010), phase-change materials (Jegadheeswaran & Pohekar 2009; Hu *et al.* 2022; Choure, Alam & Kumar 2023), and the behaviour of icy satellites (Spencer *et al.* 2006; Kang & Flierl 2020). Accurately estimating melt and freeze rates of ice is crucial for understanding and predicting changes in polar ice, which has direct implications for global climate dynamics (Manabe & Stouffer 1995; Ghil & Lucarini 2020), geoscience (Magorrian & Wells 2016; Moon *et al.* 2018) and astrophysics (Butcher *et al.* 2017; Kang *et al.* 2022). However, the two-way interaction between the moving solid–liquid boundary and the surrounding turbulent flow makes these processes highly complex and difficult to model. Extensive research has explored how various types of turbulent flows interact with solid surfaces during both melting and freezing processes (Davis, Müller & Dietsche 1984; Dietsche & Müller 1985; Esfahani *et al.* 2018; Favier, Purseed & Duchemin 2019; Couston *et al.* 2021; Wang *et al.* 2021*b*; Yang *et al.* 2023*b*). Studies have focused on interface patterns, equilibrium states, and the intricate dynamics of phase boundaries under freezing and melting conditions, as also summarised in the recent comprehensive review by Du, Calzavarini & Sun (2024).

In realistic environments, melting and freezing often alternate depending on external conditions, such as daily and seasonal solar cycles that affect sea ice (Perovich & Polashenski 2012), or periodic heating and cooling cycles that influence phase-change materials (Choure *et al.* 2023; Yang *et al.* 2024) and asymmetric external forces that regulate phase change thermal management (Hu & Fan 2023; Hu *et al.* 2025). This alternation between melting and freezing raises intriguing questions regarding symmetry and reversibility. As a fundamental Stefan problem (Rubinstein 1971), one might expect phase transformations to exhibit symmetry – melting as the inverse process of freezing – resulting in a final state that is independent of the initial conditions (Ristroph 2018). However, ambient flows can break this symmetry, giving rise to complex and even bistable equilibrium states. For example, solar-heated melt ponds in polar regions can exhibit bistability, where the final pond state depends on its initial depth (Yang *et al.* 2023*a*).

Similarly, in the system of Rayleigh–Bénard (RB) convection (Ahlers, Grossmann & Lohse 2009; Lohse & Xia 2010; Chillà & Schumacher 2012; Lohse & Shishkina 2023, 2024) – a configuration in which a fluid is heated from below and cooled from above – melting and freezing processes can also yield multiple equilibrium states (Purseed *et al.* 2020). In cases where the melting temperature lies between the temperatures of the top and bottom plates, numerical studies have shown that the interface may settle into one of two distinct states: a diffusive state or a convective state, depending on initial conditions (Purseed *et al.* 2020). Based on this, one might hypothesise that this bistability would disappear in highly turbulent flows, leaving only a single convective equilibrium state. However, earlier experimental studies observed two distinct convective states with different interface patterns during melting and freezing, suggesting a persistent influence of initial conditions even in turbulent regimes (Dietsche & Müller 1985). Recent experiments by Wang *et al.* (2021*a*) have further revealed that the morphology of ice in an RB set-up depends sensitively on the aspect ratio of the container, underscoring the possibility of multiple stable states under identical external conditions. These findings highlight the complexity of the underlying mechanisms and the need for deeper investigation. Understanding the physical mechanisms behind these observations is critical, as they have implications not only for geophysical and industrial applications, but

also for fundamental questions about symmetry-breaking and pattern formation in fluid systems. Further research in this area could improve predictive models of phase-change dynamics in turbulent environments.

In this paper, we present direct numerical simulations (DNS) of melting and freezing in the presence of turbulent convection, aiming to elucidate the asymmetry between these two phase-change processes induced by convective flow. We mainly focus on the equilibrium interface height for melting and freezing, which is an important physical property of the system since it is linked to the heat fluxes by considering the heat flux balance across the solid–liquid interface. In particular, we want to understand the dependence on the control parameters. Our work bridges previous experimental findings with new numerical possibilities and insights, revealing the asymmetry of morphology, equilibrium interface heights, and that corresponding heat flux between melting and freezing indeed persists over a broad range of control parameters. We show that the presence of convective flow disrupts the symmetry, and both qualitative and quantitative analyses suggest that this asymmetry arises from the history-dependent behaviour of the convective flow. The existence of multiple stable states indicates that the exact configuration of the solid–liquid interface is influenced not only by the surrounding environmental conditions, but also by its evolution history. Additionally, we propose a physical model that captures this asymmetry, providing predictions for the equilibrium interface height in both melting and freezing processes. This model advances our understanding of the dynamic interaction between turbulent flows and phase-change interfaces.

The rest of the paper is organised as follows. The set-up and the DNS are introduced in § 2. The numerical results on the asymmetric flow structure and the equilibrium states are discussed in § 3. A theoretical model is provided in § 4. Finally, conclusions and an outlook are presented in § 5.

2. Set-up and control parameters

The simulations are carried out using the Navier–Stokes equations within the Boussinesq approximation and the advection–diffusion equation and heat transfer, and the phase-field equation for the phase transition, commonly used to numerically investigate melting and freezing processes in recent studies (Favier *et al.* 2019; Hester *et al.* 2020; Yang *et al.* 2023*c*; Du *et al.* 2024). For $Pr \geqslant 1$, as is relevant here, there are very close similarities between two-dimensional (2-D) and three-dimensional (3-D) RB flows (Van Der Poel *et al.* 2013), therefore we will perform most simulations in two dimensions, also in view of our prior work (Yang *et al.* 2023*b*,*c*; Xu *et al.* 2024), which shows quantitative agreement between 2-D and 3-D simulations. We also again conducted some 3-D simulations to compare with analogous 2-D cases, finding qualitative analogies, but also some quantitative differences.

The dimensionless governing equations, constrained by the incompressibility condition $\boldsymbol{\nabla}\cdot\boldsymbol{u}=0$, are

$$\frac{\partial \boldsymbol{u}}{\partial t}+\boldsymbol{u}\cdot\boldsymbol{\nabla}\boldsymbol{u}=-\boldsymbol{\nabla}p+\sqrt{\frac{Pr}{Ra}}\,\nabla^2\boldsymbol{u}+\theta\boldsymbol{e}_z, \tag{2.1}$$

$$\frac{\partial \theta}{\partial t}+\boldsymbol{u}\cdot\boldsymbol{\nabla}\theta=\frac{1}{\sqrt{Ra\,Pr}}\,\nabla^2\theta+St\,\frac{\partial \phi}{\partial t}, \tag{2.2}$$

$$\frac{\partial \phi}{\partial t}=\frac{6}{5\,St\,C\,\sqrt{Ra\,Pr}}\left[\nabla^2\phi-\frac{1}{\epsilon^2}\phi(1-\phi)(1-2\phi+C\theta)\right]. \tag{2.3}$$

Here, the temperature field $\theta=(T-T_m)/\Delta$ has been non-dimensionalised using the temperature difference Δ between the bottom plate and the melting temperature T_m,

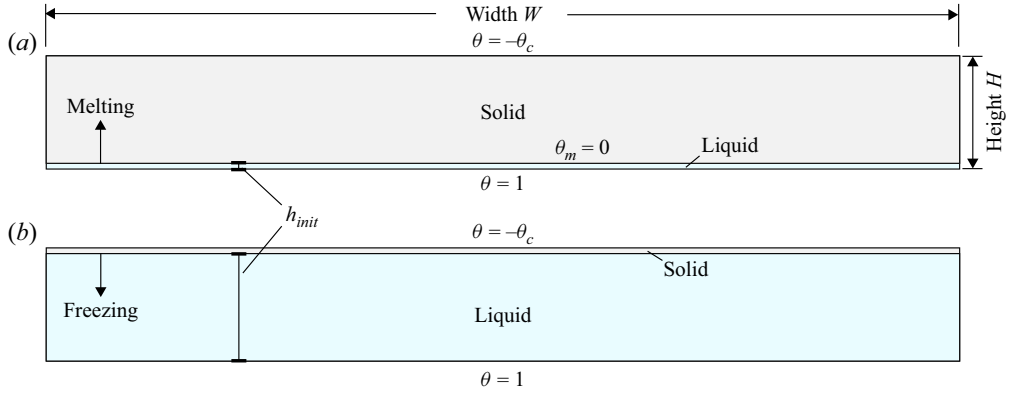

Figure 1. An illustration of the set-up and parameters with two different initial conditions: (*a*) melting case with initially mostly solid, which melts from the bottom; (*b*) freezing case with initially mostly liquid, which freezes from the top.

and the velocity field $\boldsymbol{u}$ has been non-dimensionalised with the free-fall velocity $U_f = \sqrt{g\beta H\Delta}$, where β is the thermal expansion coefficient, $\boldsymbol{e}_z$ is the direction opposite to gravity, and the velocity in the solid phase ($\phi > 0.5$) is forced to be 0. All lengths have been made non-dimensional with the plate separation H. The physical control parameters in the equations are the Rayleigh, Prandtl and Stefan numbers, domain aspect ratio, and cooling temperature at the top plate, defined as

$$Ra = \frac{\beta g \Delta H^3}{\nu\kappa}, \quad Pr = \frac{\nu}{\kappa}, \quad St = \frac{\mathcal{L}}{c_p\Delta}, \quad \Gamma = \frac{W}{H}, \quad \theta_c = \frac{T_c}{\Delta}. \tag{2.4}$$

Here, ν is the kinematic viscosity of the liquid, κ is the thermal diffusivity (which is assumed to be equal in the solid and the liquid), g is the gravitational acceleration, T_c the absolute value of the cooling temperature at the top plate, c_p is the specific heat, $\mathcal{L}$ is the latent heat, and W and H are the horizontal and vertical lengths of the domain.

The response parameters are the Nusselt number $Nu = QH/(K\Delta)$ and the Reynolds number $Re = UH/\nu$, which indicate the dimensionless heat transport and flow strength in the system. Here, Q is the heat flux crossing the system, $K = \kappa\rho c_p$ is the thermal conductivity in the liquid phase, and $U = \sqrt{\langle u^2\rangle_V}$ is the time and volume averaged root mean square (r.m.s.) velocity. Note that the thermal diffusivities and conductivities in liquid and solid are the same in our simulations. We also quantify the interface morphology by the spatial-averaged interface height $\overline{h}$ and the wavenumber of the cellular structure at the interface k.

The simulation set-up is illustrated in figure 1(*a*,*b*). We apply two different initial conditions to explore the melting and freezing dynamics: a predominantly solid phase for the melting case (initially 95 % solid, as shown in figure 1*a*), and a predominantly liquid phase for the freezing case (initially 95 % liquid, shown in figure 1*b*). The temperature boundary conditions are set to a fixed temperature $\theta = 1$ at the bottom plate, $\theta = -\theta_c$ at the top plate, and $\theta = 0$ for the melting/freezing temperature. When the top temperature is below zero, for the melting case, the solid phase gradually melts upwards from the bottom until equilibrium is reached, leaving a solid layer of a certain thickness above the liquid. For the freezing case, the liquid phase solidifies from the top until it similarly reaches an equilibrium state. For the melting case, we set the initial temperature field in the liquid to linear with random noise perturbation, and different initial settings do not affect the

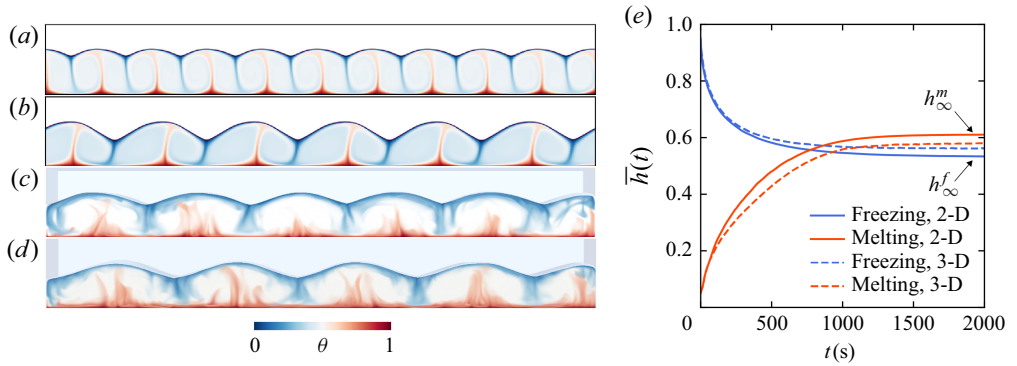

Figure 2. Instantaneous snapshots of the temperature field and the solid–liquid interface contour from 2-D simulations of (*a*) the melting case, and (*b*) the freezing case at $Ra = 10^7$, $\theta_c = 8$, and the temperature field and solid–liquid interface contour from 3-D simulations of (*c*) the melting case and (*d*) the freezing case at $Ra = 10^7$, $\theta_c = 8$. (*e*) The time evolution of the mean height $\overline{h}$ for the cases in (*a–d*).

results much due to the small proportion of the liquid phase. For the freezing case, we set the initial temperature field as

$$\theta = 1 - z/h_{init} + 1/2 \sin(2\pi k_{init}/\Gamma x) \sin(\pi z/h_{init})^2 - \theta_c(z - h_{init})/(1 - h_{init}), \tag{2.5}$$

where the initial height is set to $h_{init} = 0.95$, and the initial wavenumber is set to $k_{init} = 6$, a typical configuration on a Fourier basis that allows the flow and morphological structures to be sustained from the initial state, commonly used to control the initial number of rolls (Wang *et al.* 2020). We also further examined the effect of varying k_{init}, and found that it can lead to different final equilibrium states.

We applied periodic boundary conditions in the horizontal direction. For velocity fields, we apply no-slip at the plates. The parameter range that we will explore is for Rayleigh numbers $10^7 \leqslant Ra \leqslant 3 \times 10^8$ and for temperatures at the top plate $-40 \leqslant \theta_t \leqslant 0$. By default, Pr is set to 1 – unless specified when we investigate the effect of Pr and vary in $1 \leqslant Pr \leqslant 10$, representative of properties of the different fluid – Γ is fixed to 8, and St is fixed to 1. We also checked the effect of St for the asymmetry behaviour in Appendix A.

The DNS were performed using a finite difference code (Verzicco & Orlandi 1996) with the criteria for the grid resolution following Ostilla-Mónico *et al.* (2015). The code has been tested extensively, and benchmarked against other codes (Kooij *et al.* 2018) and applied in various fluid systems (Yang, Verzicco & Lohse 2016; Zhu *et al.* 2018; Chong *et al.* 2021; Yang *et al.* 2022). We implement the phase-field method (Hester *et al.* 2020) to simulate the melting/freezing solid (Liu *et al.* 2021). In this method, the phase-field variable ϕ is integrated in time and space, and smoothly transitions from value 1 in the solid to value 0 in the liquid. The applied phase-field model was initially derived based on entropy conservation, which guarantees the thermodynamic consistency and also satisfies the Gibbs–Thompson relation.

3. Flow structures and equilibrium states for melting and freezing

3.1. *Asymmetric flow structures and equilibrium height*

In figures 2(*a*,*b*), we present the flow structures and phase boundaries for both the melting and freezing cases under identical control parameters: $Ra = 10^7$, $\theta_c = 8$, as obtained from 2-D simulations. A clear distinction emerges in the number of thermal

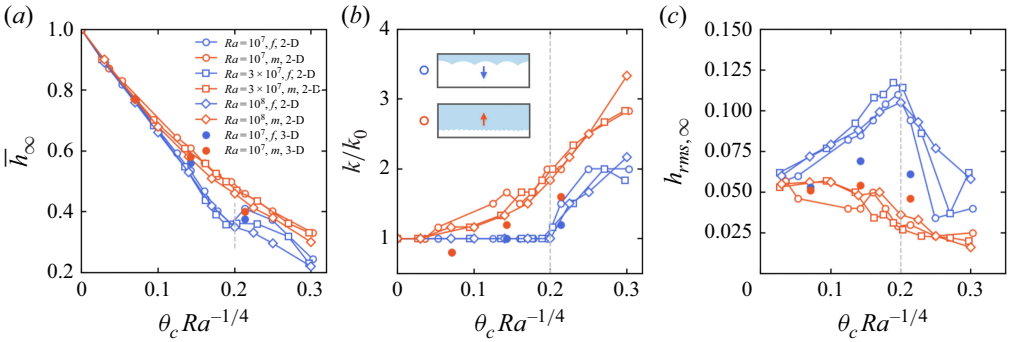

Figure 3. (*a*) The mean height $\overline{h}_\infty$ as a function of $\theta_c\, Ra^{-1/4}$ for melting and freezing cases with different Ra. The dashed line represents the location when the curves for freezing cases transition to increase. (*b*) The wavenumber k/k_0 as a function of $\theta_c\, Ra^{-1/4}$ for melting and freezing cases with different Ra, where k_0 is the wavenumber for $\theta_c = 0$. (*c*) The r.m.s. of the height, $h_{rms,\infty}$, as a function of $\theta_c\, Ra^{-1/4}$ for melting and freezing cases with different Ra. The dashed vertical lines in (*a–c*) are at the same value, $\theta_c\, Ra^{-1/4} = 0.2$.

plumes and the corresponding cellular patterns at the interface. This difference in flow and interface structure between melting and freezing is not limited to 2-D simulations; similar variations are also observed in 3-D simulations with $Ra = 10^7$, $\theta_c = 8$, as shown figure 2(*c*,*d*).

These differences extend beyond just flow patterns and interface wavenumbers. The final equilibrium heights $\overline{h}^m_\infty$ and $\overline{h}^f_\infty$ of the phase boundary also differ between melting and freezing processes. Figure 2(*e*) illustrates the temporal evolution of the spatially averaged interface height $\overline{h}(t)$ for both melting ($\overline{h}^m_\infty$) and freezing ($\overline{h}^f_\infty$) in the cases shown in figure 2(*a–d*). In an idealised Stefan problem with no ambient flow, one would expect both processes to reach an identical final state, controlled by the balance of heat fluxes between the solid and liquid phases. However, with convective flow, our results reveal two distinct equilibrium heights, $\overline{h}^m_\infty$ and $\overline{h}^f_\infty$, for melting and freezing, respectively. Interestingly, in the melting case, $\overline{h}^m(t)$ continues to increase over time, eventually surpassing the steadily decreasing $\overline{h}^f(t)$ observed in the freezing case, so that $\overline{h}^m_\infty > \overline{h}^f_\infty$.

This difference in the equilibrium heights $\overline{h}^m_\infty$ and $\overline{h}^f_\infty$ highlights an asymmetry induced by the convective flow, which is a marked difference from traditional Stefan problem expectations. The presence of buoyancy-driven flow not only modifies the flow-field structure and interface geometry, but also influences the overall phase-change dynamics, leading to different thermal equilibria. This finding underscores the critical role of convective effects in breaking the symmetry between melting and freezing, suggesting that the history and intensity of convective flows can have lasting impacts on the final interface configuration, which is relevant to a variety of natural and industrial applications.

3.2. *Asymmetry dependence on Ra and initial condition*

The observed asymmetry between melting and freezing is evident across a broad range of Rayleigh numbers Ra and cooling temperatures θ_c. In figure 3(*a*), we plot the equilibrium mean interface heights $\overline{h}^m_\infty$ and $\overline{h}^f_\infty$ as functions of the rescaled parameter $\theta_c\, Ra^{-1/4}$ across various values of Ra and θ_c. This rescaling is based on the heat flux balance at the interface, as well as the classical heat transfer scaling $Nu \sim Ra^{1/4}$ from Grossmann–Lohse theory (Grossmann & Lohse 2000, 2001), which compensates for the effect of Ra,

and facilitates a clearer comparison between cases. Consistently, the melting cases exhibit higher values of $\overline{h}_\infty$ than the freezing cases under the same conditions of Ra and θ_c, i.e. $\overline{h}^m_\infty > \overline{h}^f_\infty$. Notably, the difference in $\overline{h}_\infty$ between the melting and freezing cases increases with larger values of θ_c, and decreases with decreasing $\overline{h}_\infty$. Beyond a certain threshold of θ_c, however, this difference begins to diminish. This is because when the liquid layer becomes sufficiently shallow, and the flow approaches a laminar state, the differences between the melting and freezing cases eventually vanish. At higher Ra, the effective Ra remains larger for the same $\overline{h}_\infty$, meaning that the differences persist until $\overline{h}_\infty$ becomes even smaller, or θ_c becomes even larger. We will analyse this in further detail in the following subsections.

Figure 3(*b*) presents the wavenumber k of the cellular structure at the interface as a function of $\theta_c\, Ra^{-1/4}$. Here again, the melting cases show consistently higher wavenumbers than the freezing cases for identical values of Ra and θ_c, with k increasing as θ_c rises. This correlation between $\overline{h}^{m,f}_\infty$ and k reflects a broader trend: systems with a larger number of convection rolls exhibit enhanced heat transport properties, as seen in prior studies on RB convection (Wang *et al.* 2020) and Taylor–Couette flow (Huisman *et al.* 2014). Based on the heat flux balance between the liquid and solid phases, improved heat transport within the liquid phase translates to a higher equilibrium height $\overline{h}^m_\infty$ during the melting process.

Note that the statistics for the freezing cases in figure 3(*b*) appear to be more chaotic at higher cooling temperatures. This is because, as the cooling temperature increases, splitting events occur intermittently, allowing k to remain approximately constant within a certain range of θ_c until the next splitting event occurs. Furthermore, at higher cooling temperatures, the fluid layer becomes shallower, and the flow weakens, resulting in longer time scales for new splitting events to develop.

Figure 3(*c*) shows the morphology roughness, represented by the r.m.s. of the height, $h_{rms,\infty}$, as a function of $\theta_c\, Ra^{-1/4}$. The freezing cases show consistently rougher interfaces than the melting cases, given the same control parameters. Meanwhile, for the freezing cases, $h_{rms,\infty}$ shows a non-monotonic trend. As θ_c increases, $h_{rms,\infty}$ first increases and then decreases, with the same transition location as the increase of k. Note that there is a difference between the 2-D and 3-D results. The difference between freezing and melting is relatively smaller in three dimensions than in two, likely due to flow patterns in the third direction destabilising the 2-D circulation, leading to merging and splitting events. This effect reduces the observed wavenumber difference between melting and freezing cases. However, we believe that the difference in equilibrium heights between freezing and melting remains robust, as it has also been observed in experiments. For instance, Dietsche & Müller (1985) reported 12 cells in the freezing case, and 15 cells in the melting case, under identical control parameters. Similarly, Wang *et al.* (2021*a*) demonstrated that multiple stable ice profiles can emerge, corresponding to different convective states under the same external conditions. Furthermore, we will present a model based on heat flux balance to quantitatively unify all results in § 4, including both 2-D and 3-D results.

To explore the role of the initial flow structure in the freezing cases, we performed additional tests by initialising the freezing cases with varying numbers of rolls, each corresponding to a different initial wavenumber k_{init}. These cases demonstrate that the initial morphology can indeed be sustained, with the number of rolls persisting through the evolution, as illustrated in figure 4(*a–d*). In figure 4(*e*), we plot $\overline{h}^f_\infty$ as function of $\theta_c\, Ra^{-1/4}$ for different initial roll numbers k_{init}, revealing an intriguing trend: the threshold

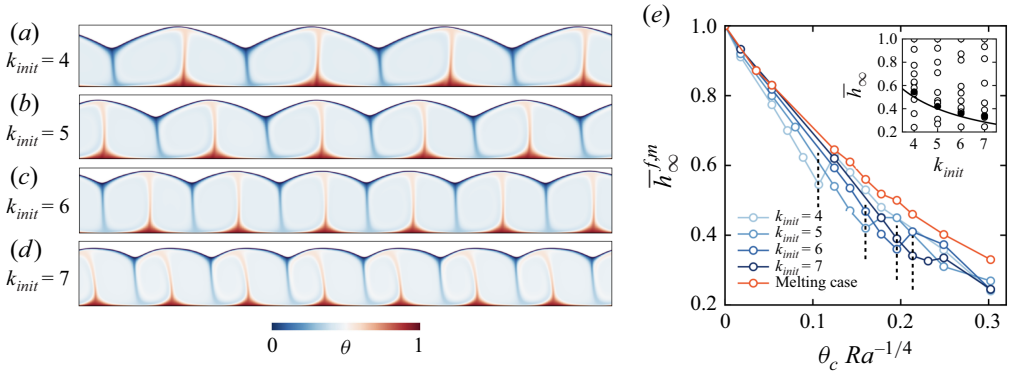

Figure 4. (*a–d*) Instantaneous snapshots of temperature fields with the solid–liquid interface contour for different k_{init} at $Ra = 10^7$ at the equilibrium stage. (*e*) The mean height $\overline{h}^{f,m}_{\infty}$ as a function of $\theta_c\, Ra^{-1/4}$ for freezing cases with different k_{init}, and the melting case, at $Ra = 10^7$. The dashed lines show the locations where the curves for freezing cases transition and increase. We also include the melting case $\overline{h}^{m}_{\infty}$. The inset represents $\overline{h}^{f}_{\infty}$ as a function of k_{init}. The black points represent the transition points, and the solid line represents the prediction from (3.2).

of θ_c for the transition in the freezing curve and the associated $\overline{h}^{f}_{\infty}$ vary depending on the initial wavenumber, as depicted in the inset in figure 4(*e*). This resembles the case of standard RB turbulence, for which Wang *et al.* (2020) showed that for a given aspect ratio and Ra, Pr, only a certain number of rolls form a stable equilibrium.

We further test different initial conditions for the freezing case by setting the flow with various numbers of rolls initially. Given a certain number of rolls k_{init} initially, the morphology can be adjusted and sustained to follow the number of rolls, as shown in figure 4(*a–d*). Figure 4(*e*) shows $\overline{h}^{f,m}_{\infty}$ as a function of $\theta_c\, Ra^{-1/4}$ with different initial number of rolls. Interestingly, these cases show the transition at different θ_c and corresponding $\overline{h}^{f}_{\infty}$, which is also shown in the inset.

3.3. *Equilibrium states predicted by the critical aspect ratio Γ_c*

The stability of initial conditions can be quantified by the aspect ratio of the convection cells, denoted $\Gamma_c = \Gamma/(k\overline{h}_{\infty})$. For the transient melting processes in RB convection, Yang *et al.* (2023*c*) showed that Γ_c is bounded within a specific range, constrained by the elliptical instability criteria for convection cells (Wang *et al.* 2020; Zwirner, Tilgner & Shishkina 2020). In brief, the strain–vorticity balance in 2-D flows is determined by the (elliptical) shape of the rolls. The aspect ratio of the rolls is directly related to the strain and the vorticity. To form a roll, the strain must be bounded by the vorticity, which gives the limits of Γ_c. This range provides theoretical lower and upper bounds for the aspect ratio that allow stable convection patterns within the system. Yang *et al.* (2023*c*) further showed that the merging events in melting cases occur when the aspect ratio decreases until it reaches the lower bounds.

We examine these bounds in the equilibrium state by analysing the equilibrium structure of the solid–liquid interface for various control parameters. Figure 5 illustrates Γ_c as a function of Ra_{eff} for both melting and freezing cases, where $Ra_{eff} = \alpha g \Delta \overline{h}^{3}_{\infty}/(\nu\kappa)$ is the effective Rayleigh number, which serves as an essential measure of the effective buoyancy-driven convection strength in the system. The plot reveals two distinct boundaries, with theoretical bounds derived based on the work of Shishkina (2021),

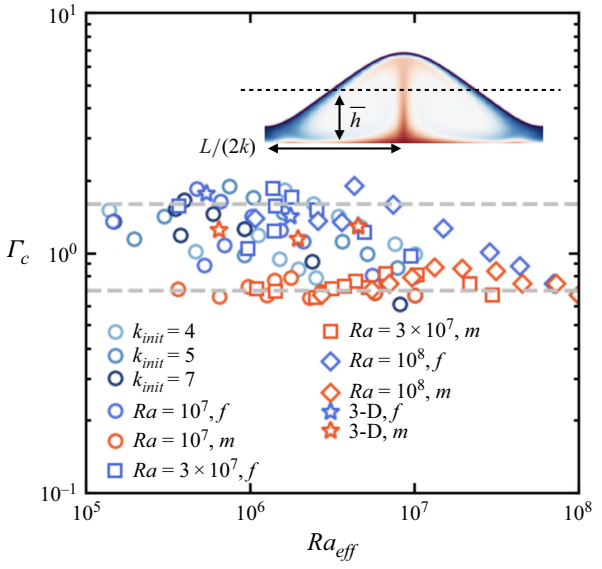

Figure 5. The aspect ratio Γ_c as a function of the effective Rayleigh number Ra_{eff} for all simulation cases.

which gives

$$\Gamma_{c1} \lesssim \Gamma_c \lesssim \Gamma_{c2}, \tag{3.1}$$

where $\Gamma_{c1} = 0.7$ and $\Gamma_{c2} = 1.6$ are independent of Ra_{eff}. For the same control parameters, the aspect ratios in the melting cases tend to be lower and closer to the lower bound compared to those in the freezing cases. This finding aligns with our observations of distinct equilibrium heights and wavenumber characteristics in the two processes in figure 3. Melting cases favour compact convection cells with lower aspect ratios due to the growth and merging from small plumes, while freezing cases tend to maintain the elongated cells with higher aspect ratios from the initial large plumes, indicative of differing heat transport efficiencies.

This analysis also provides insight into the possible range of initial wavenumbers, as the system's behaviour is constrained within these theoretical bounds of Γ_c. For initial states falling within the lower and upper bounds, stable roll structures are more likely to form, while initial conditions outside this range lead to unstable or transitional flow patterns.

3.4. *Asymmetry dependence on Pr*

Another important control parameter in this study is the Prandtl number Pr, which we have fixed as 1 to maintain consistency. However, in real-world applications, Pr depends on fluid properties that can vary significantly, such as reaching value $Pr = 10$ for cold water near 0 °C. Figure 6 shows the effect of varying Pr from 1 to 10 on the observed asymmetry in melting and freezing behaviours. Notably, as Pr increases, the asymmetry between melting and freezing becomes less pronounced, and ultimately vanishes at $Pr = 10$, as depicted in figure 6(*d*), which means that for ice melting in cold water, this asymmetry should be negligible.

The changes in flow structure at different Pr values shed light on this phenomenon. At $Pr = 1$, as shown in figure 6(*a*), the flow is more coherent, with a circulation-dominated structure that supports large-scale convective rolls. This organised flow pattern promotes distinct cellular structures at the solid–liquid interface, enhancing the asymmetry

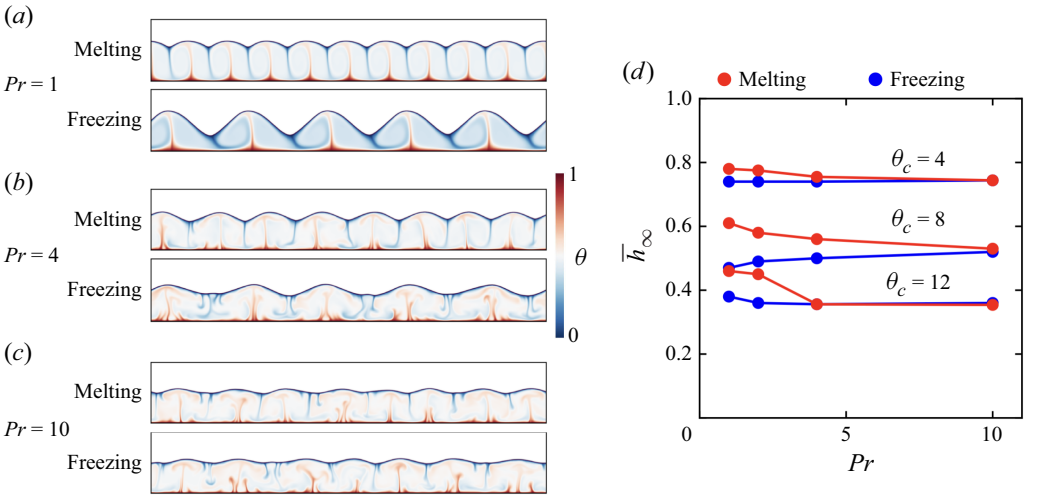

Figure 6. The effect of Prandtl number. The 2-D simulations of melting and freezing cases at $Ra = 10^7$ and (*a*) $Pr = 1$, (*b*) $Pr = 4$, (*c*) $Pr = 10$. (*d*) The mean height $\overline{h}_\infty$ as a function of Pr for different θ_c, for both melting and freezing.

between melting and freezing. However, as Pr increases, the flow becomes more and more chaotic (see figure 6*b*,*c*), with increasing number of plumes, and disrupting the large-scale circulation. Smaller plume-dominated structures emerge, creating a more randomised and chaotic flow. In this scenario, the melting case, which initially has more cells, tends to experience merging events, reducing the total number of cells. Conversely, in the freezing case, where fewer cells are present, splitting events may occur, increasing the number of cells. As a result, the contrast between melting and freezing cases diminishes as the flow self-reorganises dynamically, leading to less asymmetry between the two cases at higher Prandtl numbers.

This shift from coherent to chaotic flow with higher Pr underscores the influence of the fluid properties on phase-change processes. A high Pr inhibits the development of stable cellular patterns, resulting in a loss of the organised structure that initially drives the asymmetry. As a result, for applications where Pr is naturally high, such as in cold-water dynamics, the distinction between melting and freezing dynamics may be less evident. However, it requires a more comprehensive exploration of the parameter space for different Pr to fully understand the effect of Pr, including the influence of Pr at different θ_c. In the remainder of this study, we maintain $Pr = 1$ to focus on the regime where asymmetry is most pronounced, and examine the underlying mechanisms in more detail.

3.5. *Convection cell splitting events in freezing cases*

Another intriguing aspect of this study is the complex evolution observed in the freezing case. While the melting dynamics has been well-documented in the literature, with studies showing that the solid continuously melts as underlying plumes grow, merge and restructure (Favier *et al.* 2019; Yang *et al.* 2023*c*), the freezing process exhibits distinctive, non-monotonic behaviour, particularly when θ_c is sufficiently high. As shown in figure 7(*b*), the evolution of the mean interface height $\overline{h}^f(t)$ during freezing displays a non-monotonic trend, indicating a series of dynamic structural transitions that are not present in the melting case. Similar behaviour for $h_{rms,\infty}$ can be seen in figure 7(*c*,*d*).

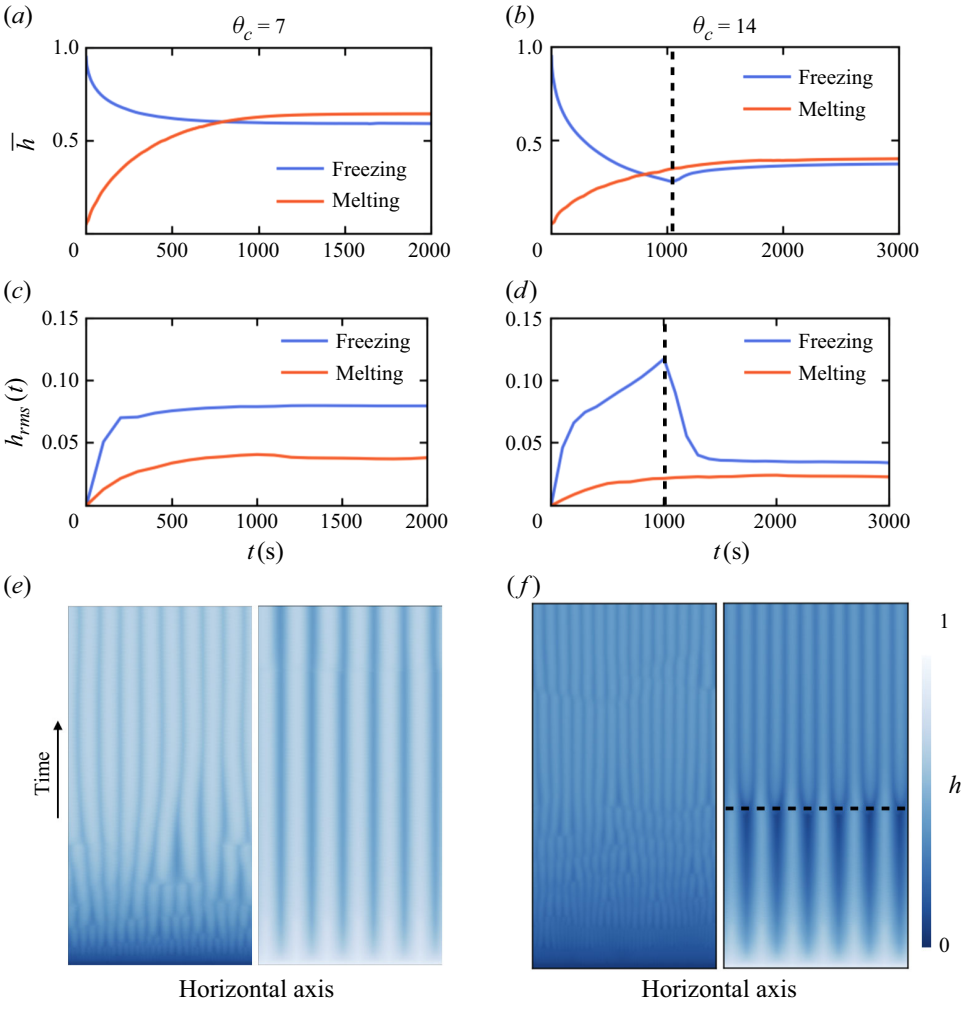

Figure 7. The temporal evolution of the mean height $\overline{h}$ for melting and freezing cases at the same control parameters: (*a*) $Ra = 10^7$, $\theta_c = 7$, and (*b*) $Ra = 10^7$, $\theta_c = 14$. In both cases, $Pr = 1$. The dashed line in (*b*) represents the time when the curve of the freezing case starts to increase. (*c*,*d*) The temporal evolution of h_{rms} for melting and freezing cases at the same control parameters. The temporal evolution of the interface height $h(x)$ for melting (left) and freezing (right) cases at (*e*) $Ra = 10^7$, $\theta_c = 7$, and (*f*) $Ra = 10^7$, $\theta_c = 14$. The horizontal dashed line in (*f*) represents the same time as in (*b*) and (*d*) when the curve of the freezing case starts to increase.

To gain further insight into this feature, we examine the temporal evolution of the interface height for both melting and freezing cases, presented in figure 7(*e*,*f*). At $\theta_c = 7$, the melting case shows the expected merging of convection cells over time until a stable equilibrium state is achieved. In contrast, the freezing case maintains a stable cellular pattern from start to finish, with no significant changes in cell number or arrangement. However, at a larger top cooling temperature, $\theta_c = 14$, for the melting case, convection rolls continue to exhibit merging behaviour. Interestingly, for the freezing case, convection rolls undergo a notable 'splitting' event, where existing cellular structures divide, forming additional cells. This splitting corresponds to a point in time when $\overline{h}^f(t)$ begins to increase, indicating a secondary phase in the freezing process.

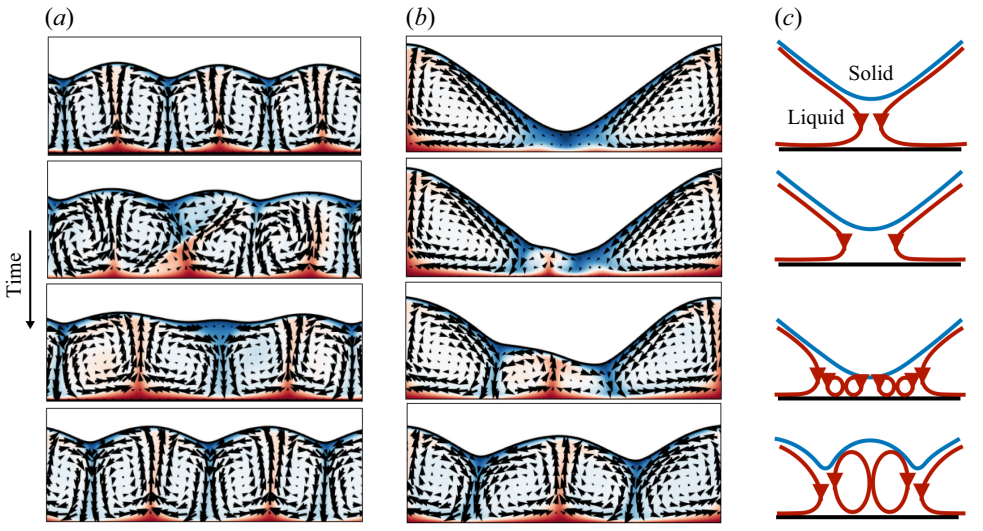

Figure 8. Zoom-in (height from 0 to 0.5) snapshots of the temperature field, the velocity vectors, and the solid–liquid interface contour for (*a*) melting and (*b*) freezing cases at $Ra = 10^7$, $\theta_c = 14$. From top to bottom represents the time evolution of merging cells for the melting case, and splitting cells for the freezing case. (*c*) Illustrations of the splitting cell event for the freezing case.

The nature of these splitting events becomes clearer when we examine the flow and temperature fields, as illustrated in figure 8. Figure 8(*a*) depicts the convection roll merging process over time during melting, while figure 8(*b*) focuses on the convection roll splitting dynamics during freezing. Consistent with prior studies (Favier *et al.* 2019; Yang *et al.* 2023*c*), the cellular structures at the interface are supported by the convective plumes and circulatory flow underneath. In the melting case, the stronger heat flux from rising hot plumes compared to sinking cold plumes results in a more pronounced melt rate beneath each convection cell. As melting progresses, plumes can grow and destabilise, leading to the merging of adjacent cells.

In contrast, during the freezing process, a different mechanism emerges when θ_c is high enough. As the solid phase advances towards the bottom plate, it creates a thin, weak-flow region close to the solid–liquid boundary. This region provides a low-shear environment that helps the formation of new plumes. As these new plumes grow, they efficiently enhance heat transport, increasing the local heat flux and leading to further melting, forming a new cellular structure. As the cell continues to melt and grow, it eventually merges into a larger roll, effectively 'splitting' the existing cells at the interface. Figure 8(*c*) illustrates this convection roll splitting phenomenon, which occurs only when θ_c reaches a threshold that brings the freezing front into close proximity with the bottom plate. This splitting behaviour in the freezing case underscores a key difference in the underlying mechanisms governing melting and freezing in convective environments. While melting processes predominantly result in the merging of convection cells, freezing introduces conditions that facilitate cell division and increased structural complexity. This difference in behaviour at higher θ_c values is a direct outcome of the two-way coupling between the phase boundary and the convective flow.

We further provide a theoretical model to predict the occurrence of convection roll splitting events. The non-monotonic behaviour of the $\overline{h}^f(t)$ in freezing cases is due to the splitting of convection rolls, which enhances the heat flux, leading to an intermediate increase in $\overline{h}^f(t)$. The splitting is caused by the instability of convection rolls. As the

solid keeps freezing, $\overline{h}^f(t)$ decreases, and the instantaneous aspect ratio increases until it reaches the upper limit and cannot be sustained any longer, then the splitting event occurs. Therefore, the splitting of convection rolls is directly related to the stability of these rolls, and can be predicted from the critical aspect ratio Γ_c in (3.1). This critical upper bound explains the occurrence of splitting events in the freezing cases, and gives a prediction for the critical height $\overline{h}_c$ when the splitting event occurs as a function of the initial wavenumber k_{init}, as

$$\overline{h}_c = \frac{\Gamma}{\Gamma_{c2} k_{init}}, \tag{3.2}$$

which is plotted in the inset of figure 4(*b*), and shows good agreement with the transition points (corresponding to when the splitting event occurs) in numerical simulations.

4. Unifying model for the equilibrium state $\overline{h}_\infty$ as a function of θ_t, Ra and Γ_c

Building on the introduced effective Rayleigh number Ra_{eff} and the cell aspect ratio Γ_c, we further propose a unifying model to predict the mean height $\overline{h}_\infty$ under varying θ_t, Ra and Γ_c. The equilibrium height can be derived from the heat flux balance across the solid–liquid interface, expressed as

$$Nu \frac{1}{\overline{h}_\infty} = \frac{\theta_c}{1-\overline{h}_\infty}, \tag{4.1}$$

where the term on the left-hand side represents the heat flux in the liquid phase, and the term on the right-hand side corresponds to the heat flux in the solid phase. Here, Nu remains unknown and needs to be determined to solve for $\overline{h}_\infty$.

In classical RB convection, Nu can be well predicted using the Grossmann–Lohse theory, which predicts $Nu \sim Ra^{1/4}$ for the range of Ra and Pr used in our study. Furthermore, to account for the effect of Γ_c, we modify this scaling relationship by assuming that Nu has a linear dependence on Γ_c. We acknowledge that this linear dependence does not hold universally, and refer to Shishkina (2021) for a more detailed analysis of the Nu dependence on Γ_c. However, in our parameter space, plotting the rescaled quantity $Nu\, Ra^{-1/4}$ against Γ_c reveals a linear trend, and the same for $Re\, Ra^{-1/2}$ against Γ_c, as shown in the insets of figure 9(*a*,*b*), allowing us to approximate Nu as

$$Nu = a_0\, Ra_{eff}^{1/4}\, Pr^{-1/12}\, f_{Nu}(\Gamma_c), \tag{4.2}$$

$$Re = b_0\, Ra_{eff}^{1/2}\, Pr^{-1}\, f_{Re}(\Gamma_c), \tag{4.3}$$

where $f_{Nu}(\Gamma_c) = 1 - a_1(\Gamma_c - \Gamma_{c0})$ and $f_{Re}(\Gamma_c) = 1 - b_1(\Gamma_c - \Gamma_{c0})$ are linear functions of Γ_c, with Γ_{c0} fixed as 1, corresponding to the typical aspect ratio for the Grossmann–Lohse theory. The constants a_0 and b_0 are empirically determined coefficients, and a_1 and b_1 represent the sensitivity of Nu and Re to variations in Γ_c, which are obtained by the fitting of the simulation data.

To validate this model for the Γ_c dependence, we plot the compensated quantities $Nu\, f_{Nu}^{-1}$ and $Re\, f_{Re}^{-1}$ as functions of Ra_{eff} in figure 9(*a*,*b*). The results show that across a range of cases, the data collapse onto a single scaling curve, as predicted by (4.2) and (4.3), which supports the robustness of the linear relation between Nu, Re and Γ_c for the parameter space in our study.

By combining (4.1) and (4.2), we derive an expression for $\overline{h}_\infty$:

$$\overline{h}_\infty^{-1/4}(1-\overline{h}_\infty) = \theta_c\, Nu_0^{-1}\, f_{Nu}^{-1}(\Gamma_c), \tag{4.4}$$

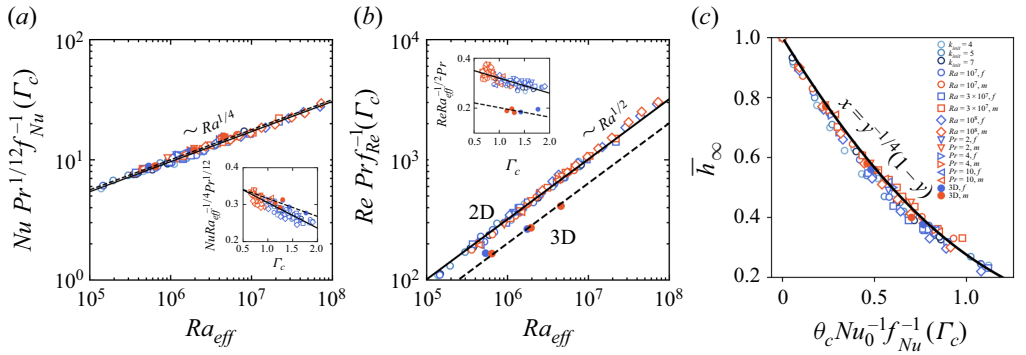

Figure 9. (*a*) Plot of $Nu\ f_{Nu}^{-1}$ as a function of Ra_{eff} from various numerical simulations; see legend in (*c*). The solid line shows the scaling relation of (4.2), and the inset shows $Nu\ Ra^{-1/4}$ against Γ_c, with the solid line being the linear fitting. (*b*) Plot of $Re\ f_{Re}^{-1}$ as a function of Ra_{eff}. The solid line is the scaling relation (4.3), and the inset shows $Re\ Ra^{-1/2}$ against Γ_c, with the solid line being the linear fitting. (*c*) The equilibrium interface height $\overline{h}_\infty$ as a function of $\theta_c\ Nu_0^{-1}\ f_{Nu}^{-1}(\Gamma_c)$ based on (4.4).

where $Nu_0 = a_0\ Ra_{eff}^{1/4}$. In figure 9(*c*), we plot $\overline{h}_\infty$ as a function of the rescaled cooling temperature $\theta_c\ Nu_0^{-1}\ f_{Nu}^{-1}(\Gamma_c)$. The black line represents the theoretical prediction from (4.1), showing excellent agreement with the simulation data.

5. Conclusion and outlook

In conclusion, this study provides a detailed investigation into the asymmetric behaviours of melting and freezing processes in RB convection, revealing distinct differences in the equilibrium flow structures, solid–liquid interface morphology, and the equilibrium mean interface heights $\overline{h}_\infty^m$ and $\overline{h}_\infty^f$. Our results demonstrate that this asymmetry is robust across a wide range of Rayleigh numbers Ra and top cooling temperatures θ_c, indicating that the convective dynamics plays a critical role in breaking the symmetry between these phase-change processes. A close examination of the morphological evolution in the freezing cases reveals the occurrence of a convection roll splitting event in the cellular structures at the interface, which accounts for the observed non-monotonic trend in the height evolution. This convection roll splitting, absent in the melting cases, provides insights into the role of convective instabilities and plume dynamics in shaping the solid–liquid boundary during freezing. Such events lead to the formation of additional convective cells, and explain the sustained difference in interface height between the two processes.

To quantify these morphological differences, we have introduced an effective aspect ratio Γ_c of the cellular structures at the interface, which is shown to be constrained between theoretical upper and lower bounds derived from the convection roll stability criteria of Wang *et al.* (2020) and Shishkina (2021). The observed aspect ratio bounds align with theoretical predictions, reinforcing the idea that the convective cell structure in the liquid phase strongly influences the overall interface morphology. Finally, using the Grossmann–Lohse theory and the heat flux balance, we develop a unifying model that accurately predicts the equilibrium interface height $\overline{h}$ across various initial conditions and control parameters. The resulting predictions are consistent with our numerical results, successfully capturing the trends in $\overline{h}_\infty$ across melting and freezing cases, $\overline{h}_\infty^m$ and $\overline{h}_\infty^f$.

These findings advance our understanding of the complex interactions between phase-change dynamics and convective flow, highlighting the importance of historical flow states

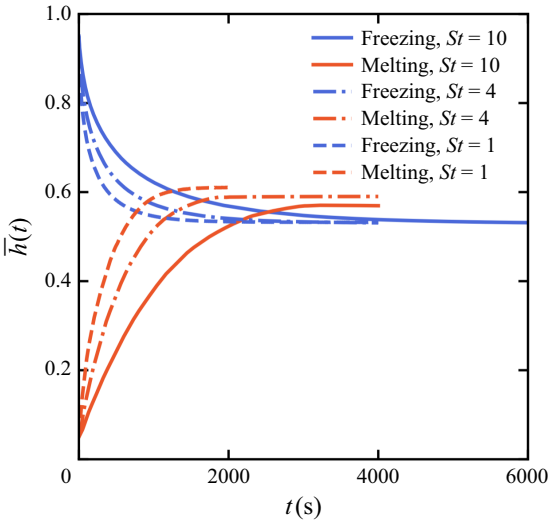

Figure 10. Temporal evolution of $\overline{h}(t)$ at $Ra = 10^7$, $Pr = 1$ and $\theta_c = 8$ for different St.

and morphological evolution in determining the final equilibrium conditions. This work not only extends existing models of convective phase change by accounting for asymmetry in melting and freezing, but also provides a framework for exploring similar behaviours in more complex, 3-D systems and applications involving phase-change materials and thermal management technologies.

Future studies could explore how varying boundary conditions (Yang *et al.* 2024), initial conditions (Purseed *et al.* 2020; Wang *et al.* 2021*a*), external forces (Couston *et al.* 2021) and saline concentration (Du *et al.* 2023; Xue, Zhang & Ni 2024), as well as freshwater temperature with density anomaly effect (Wang *et al.* 2021*b*), further influence the symmetry-breaking mechanisms in convective melting and freezing, as well as the merging and splitting events. The persistence of asymmetry at higher Ra also warrants further investigation, as the increasingly chaotic plume and circulation patterns may diminish the differences between the melting and freezing cases, similar to the observed trends at high Pr.

Funding. This work was financially supported by the European Union (ERC, MultiMelt, 101094492). It was carried out on the Dutch national e-infrastructure with the support of SURF Cooperative. We also acknowledge the EuroHPC Joint Undertaking for awarding the project EHPC-REG-2023R03-178 access to the EuroHPC supercomputer Discoverer.

Declaration of interests. The authors report no conflict of interest.

Appendix A. The effect of St on the asymmetric melting and freezing

Considering that the Stefan number St is different in realistic cases as we have modelled here ($St = 1$ for computational efficiency), we conducted additional simulations with $St = 10$ (e.g. ice melting in 8 °C water) and $St = 4$ (e.g. ice melting in 20 °C water) at $Ra = 10^7$, $Pr = 1$ and $\theta_c = 8$ to examine the influence of St on the melting and freezing processes. Figure 10 presents the temporal evolution of the spatially averaged interface height $\overline{h}(t)$ for these cases. As anticipated, the time required to reach equilibrium increases with a larger St, reflecting the larger energy needed for phase change under higher St conditions. This energy requirement leads to a slower rise of $\overline{h}_\infty$ during melting, which,

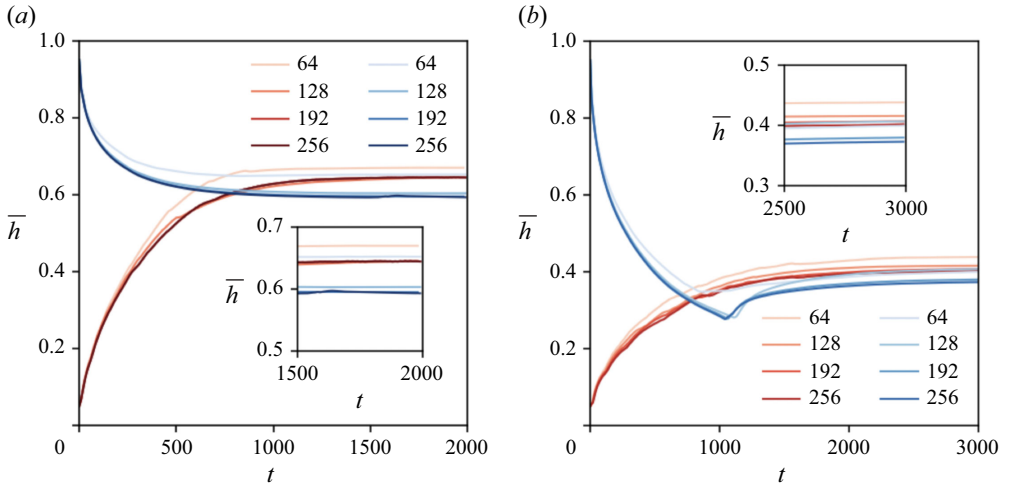

Figure 11. Temporal evolution of $\overline{h}(t)$ at $Ra = 10^7$, $Pr = 1$ and (*a*) $\theta_c = 7$, (*b*) $\theta_c = 14$, for different vertical resolutions. The blue lines represent the freezing cases, and the red lines represent the melting cases. The horizontal resolution is determined by multiplying the vertical resolution by the domain aspect ratio.

in turn, allows more time for plume merging and reorganisation, ultimately resulting in a lower equilibrium wavenumber k and a slightly reduced final $\overline{h}_\infty$.

Despite these effects on the dynamics, the asymmetry between melting and freezing processes persists across varying St. Both our observations and the theoretical framework that we developed remain consistent with changes in St. Thus although St affects the temporal evolution and the time scale of phase change, it does not significantly alter the underlying asymmetry in interface morphology or the flow structure between melting and freezing cases. Given this result, we have chosen to set $St = 1$ in our simulations, which allows for faster computational convergence without compromising the generality of our findings.

Appendix B. Resolution test for the evolution of mean height $\overline{h}$

To ensure the adequacy of our chosen resolution, we perform simulations at different resolutions to assess convergence, as shown in figure 11. We select $Ra = 10^7$ and $Pr = 1$ with two different θ_c, as $\theta_c = 7$ (without splitting event) and $\theta_c = 14$ (with splitting event). The results demonstrate the convergence of the temporal curve as the resolution increases. Based on this, we finalise our choice of vertical resolution as 192, constant for different Pr, and doubling it for $Ra = 10^8$.

References

Ahlers, G., Grossmann, S. & Lohse, D. 2009 Heat transfer and large scale dynamics in turbulent Rayleigh–Bénard convection. *Rev. Mod. Phys.* **81** (2), 503.

Alboussière, T., Deguen, R. & Melzani, M.B. 2010 Melting-induced stratification above the Earth's inner core due to convective translation. *Nature* **466**, 744–747.

Butcher, F.E.G., Balme, M.R., Gallagher, C., Arnold, N.S., Conway, S.J., Hagermann, A. & Lewis, S.R. 2017 Recent basal melting of a mid-latitude glacier on Mars. *J. Geophys. Res. Planets* **122** (12), 2445–2468.

Cenedese, C. & Straneo, F. 2023 Icebergs melting. *Annu. Rev. Fluid Mech.* **55**, 377–402.

CHILLÀ, F. & SCHUMACHER, J. 2012 New perspectives in turbulent Rayleigh–Bénard convection. *Eur. Phys. J. E* **35** (7), 58.

CHONG, K.L., NG, C.S., HORI, N., YANG, R., VERZICCO, R. & LOHSE, D. 2021 Extended lifetime of respiratory droplets in a turbulent vapor puff and its implications on airborne disease transmission. *Phys. Rev. Lett.* **126** (3), 034502.

CHOURE, B.K., ALAM, T. & KUMAR, R. 2023 A review on heat transfer enhancement techniques for PCM based thermal energy storage system. *J. Energy Storage* **72**, 108161.

COUSTON, L.-A., HESTER, E., FAVIER, B., TAYLOR, J.R., HOLLAND, P.R. & JENKINS, A. 2021 Topography generation by melting and freezing in a turbulent shear flow. *J. Fluid Mech.* **911**, A44.

DAVIS, S.H., MÜLLER, U. & DIETSCHE, C. 1984 Pattern selection in single-component systems coupling Bénard convection and solidification. *J. Fluid Mech.* **144**, 133–151.

DIETSCHE, C. & MÜLLER, U. 1985 Influence of Bénard convection on solid–liquid interfaces. *J. Fluid Mech.* **161**, 249–268.

DU, Y., CALZAVARINI, E. & SUN, C. 2024 The physics of freezing and melting in the presence of flows. *Nat. Rev. Phys.* **6**, 676–690.

DU, Y., WANG, Z., JIANG, L., CALZAVARINI, E. & SUN, C. 2023 Sea water freezing modes in a natural convection system. *J. Fluid Mech.* **960**, A35.

DUTRIEUX, P., STEWART, C., JENKINS, A., NICHOLLS, K.W., CORR, H.F.J., RIGNOT, E. & STEFFEN, K. 2014 Basal terraces on melting ice shelves. *Geophys. Res. Lett* **41** (15), 5506–5513.

ESFAHANI, B.R., HIRATA, S.C., BERTI, S. & CALZAVARINI, E. 2018 Basal melting driven by turbulent thermal convection. *Phys. Rev. Fluids* **3** (5), 053501.

FAVIER, B., PURSEED, J. & DUCHEMIN, L. 2019 Rayleigh–Bénard convection with a melting boundary. *J. Fluid Mech.* **858**, 437–473.

GHIL, M. & LUCARINI, V. 2020 The physics of climate variability and climate change. *Rev. Mod. Phys.* **92** (3), 035002.

GROSSMANN, S. & LOHSE, D. 2000 Scaling in thermal convection: a unifying theory. *J. Fluid Mech.* **407**, 27–56.

GROSSMANN, S. & LOHSE, D. 2001 Thermal convection for large Prandtl numbers. *Phys. Rev. Lett.* **86** (15), 3316.

HESTER, E.W., COUSTON, L.-A., FAVIER, B., BURNS, K.J. & VASIL, G.M. 2020 Improved phase-field models of melting and dissolution in multi-component flows. *Proc. R. Soc. A* **476**, 20200508.

HU, N. & FAN, L.W. 2023 Close-contact melting of shear-thinning fluids. *J. Fluid Mech.* **968**, A9.

HU, N., FAN, L.W., GAO, X. & STONE, H.A. 2025 Close-contact melting on hydrophobic textured surfaces: confinement and meniscus effects. *J. Fluid Mech.* **1010**, A46.

HU, N., LI, Z.R., XU, Z.W. & FAN, L.W. 2022 Rapid charging for latent heat thermal energy storage: a state-of-the-art review of close-contact melting. *Renew. Sustain. Energy Rev.* **155**, 111918.

HUISMAN, S.G., VAN DER VEEN, R.C.A., SUN, C. & LOHSE, D. 2014 Multiple states in highly turbulent Taylor–Couette flow. *Nat. Commun.* **5** (1), 3820.

JEGADHEESWARAN, S. & POHEKAR, S.D. 2009 Performance enhancement in latent heat thermal storage system: a review. *Renew. Sustain. Energy Rev.* **13** (9), 2225–2244.

KANG, W. & FLIERL, G. 2020 Spontaneous formation of geysers at only one pole on Enceladus's ice shell. *Proc. Natl Acad. Sci.* **117** (26), 14764–14768.

KANG, W., MITTAL, T., BIRE, S., CAMPIN, J.-M. & MARSHALL, J. 2022 How does salinity shape ocean circulation and ice geometry on Enceladus and other icy satellites? *Sci. Adv.* **8** (29), eabm4665.

KOOIJ, G.L. *et al.* 2018 Comparison of computational codes for direct numerical simulations of turbulent Rayleigh–Bénard convection. *Comput. Fluids* **166**, 1–8.

LABROSSE, S., HERNLUND, J.W. & COLTICE, N. 2007 A crystallizing dense magma ocean at the base of the Earth's mantle. *Nature* **450**, 866–869.

LIU, H.-R., NG, C.S., CHONG, K.L., LOHSE, D. & VERZICCO, R. 2021 An efficient phase-field method for turbulent multiphase flows. *J. Comput. Phys.* **446**, 110659.

LOHSE, D. & SHISHKINA, O. 2023 Ultimate turbulent thermal convection. *Phys. Today* **76** (11), 26–32.

LOHSE, D. & SHISHKINA, O. 2024 Ultimate Rayleigh–Bénard turbulence. *Rev. Mod. Phys.* **96** (3), 035001.

LOHSE, D. & XIA, K. 2010 Small-scale properties of turbulent Rayleigh–Bénard convection. *Annu. Rev. Fluid Mech.* **42** (1), 335–364.

MAGORRIAN, S.J. & WELLS, A.J. 2016 Turbulent plumes from a glacier terminus melting in a stratified ocean. *J. Geophys. Res. Oceans* **121** (7), 4670–4696.

MANABE, S. & STOUFFER, R.J. 1995 Simulation of abrupt climate change induced by freshwater input to the North Atlantic Ocean. *Nature* **378**, 165–167.

MOON, T., SUTHERLAND, D.A., CARROLL, D., FELIKSON, D., KEHRL, L. & STRANEO, F. 2018 Subsurface iceberg melt key to Greenland fjord freshwater budget. *Nat. Geosci.* **11** (1), 49–54.

OSTILLA-MONICO, R., YANG, Y., VAN DER POEL, E.P., LOHSE, D. & VERZICCO, R. 2015 A multiple-resolution strategy for direct numerical simulation of scalar turbulence. *J. Comput. Phys.* **301**, 308–321.

PEROVICH, D.K. & POLASHENSKI, C. 2012 Albedo evolution of seasonal Arctic sea ice. *Geophys. Res. Lett.* **39** (8), L08501.

VAN DER POEL, E.P., STEVENS, R.J.A.M. & LOHSE, D. 2013 Comparison between two- and three-dimensional Rayleigh–Bénard convection. *J. Fluid Mech.* **736**, 177–194.

PURSEED, J., FAVIER, B., DUCHEMIN, L. & HESTER, E.W. 2020 Bistability in Rayleigh–Bénard convection with a melting boundary. *Phys. Rev. Fluids* **5** (2), 023501.

RISTROPH, L. 2018 Sculpting with flow. *J. Fluid Mech.* **838**, 1–4.

RUBINSTEIN, L.I. 1971 *The Stefan Problem*. American Mathematical Society.

SHISHKINA, O. 2021 Rayleigh–Bénard convection: the container shape matters. *Phys. Rev. Fluids* **6** (9), 090502.

SPENCER, J.R., PEARL, J.C., SEGURA, M., FLASAR, F.M., MAMOUTKINE, A., ROMANI, P., BURATTI, B.J., HENDRIX, A.R., SPILKER, L.J. & LOPES, R.M.C. 2006 Cassini encounters Enceladus: background and the discovery of a south polar hot spot. *Science* **311**, 1401–1405.

STANTON, T.P., SHAW, W.J., TRUFFER, M., CORR, H.F.J., PETERS, L.E., RIVERMAN, K.L., BINDSCHADLER, R., HOLLAND, D.M. & ANANDAKRISHNAN, S. 2013 Channelized ice melting in the ocean boundary layer beneath Pine Island Glacier, Antarctica. *Science* **341**, 1236–1239.

VERZICCO, R. & ORLANDI, P. 1996 A finite-difference scheme for three-dimensional incompressible flows in cylindrical coordinates. *J. Comput. Phys.* **123** (2), 402–414.

WANG, Q., VERZICCO, R., LOHSE, D. & SHISHKINA, O. 2020 Multiple states in turbulent large-aspect-ratio thermal convection: what determines the number of convection rolls? *Phys. Rev. Lett.* **125** (7), 074501.

WANG, Z., CALZAVARINI, E. & SUN, C. 2021*a* Equilibrium states of the ice-water front in a differentially heated rectangular cell. *Europhys. Lett.* **135** (5), 54001.

WANG, Z., CALZAVARINI, E., SUN, C. & TOSCHI, F. 2021*b* How the growth of ice depends on the fluid dynamics underneath. *Proc. Natl Acad. Sci.* **118**, 10.

XU, D., BOOTSMA, S.T., VERZICCO, R., LOHSE, D. & HUISMAN, S.G. 2024 Buoyancy-driven flow regimes for a melting vertical ice cylinder in saline water. arXiv:2410.22050.

XUE, Z.-H., ZHANG, J. & NI, M.-J. 2024 Flow regimes in a melting system composed of binary fluid: transition from penetrative convection to diffusion. *J. Fluid Mech.* **998**, A14.

YANG, R., CHONG, K.L., LIU, H.-R., VERZICCO, R. & LOHSE, D. 2024 Melting and solidification in periodically modulated thermal convection. *J. Fluid Mech.* **998**, A10.

YANG, R., HOWLAND, C.J., LIU, H.-R., VERZICCO, R. & LOHSE, D. 2023*a* Bistability in radiatively heated melt ponds. *Phys. Rev. Lett.* **131** (23), 234002.

YANG, R., HOWLAND, C.J., LIU, H.-R., VERZICCO, R. & LOHSE, D. 2023*b* Ice melting in salty water: layering and non-monotonic dependence on the mean salinity. *J. Fluid Mech.* **969**, R2.

YANG, R., HOWLAND, C.J., LIU, H.-R., VERZICCO, R. & LOHSE, D. 2023*c* Morphology evolution of a melting solid layer above its melt heated from below. *J. Fluid Mech.* **956**, A23.

YANG, R., NG, C.S., CHONG, K.L., VERZICCO, R. & LOHSE, D. 2022 Do increased flow rates in displacement ventilation always lead to better results? *J. Fluid Mech.* **932**, A3.

YANG, Y., VERZICCO, R. & LOHSE, D. 2016 From convection rolls to finger convection in double-diffusive turbulence. *Proc. Natl Acad. Sci.* **113**, 69–73.

ZHU, X., MATHAI, V., STEVENS, R.J. A M., VERZICCO, R. & LOHSE, D. 2018 Transition to the ultimate regime in two-dimensional Rayleigh–Bénard convection. *Phys. Rev. Lett.* **120** (14), 144502.

ZWIRNER, L., TILGNER, A. & SHISHKINA, O. 2020 Elliptical instability and multiple-roll flow modes of the large-scale circulation in confined turbulent Rayleigh–Bénard convection. *Phys. Rev. Lett.* **125** (5), 054502.